Supplementary Information for: Exploring nontrivial topology at quantum criticality on a superconducting processor

Ziqi Tan,[1,2,*] Ke Wang,[2,*] Sheng Yang,[3,*] Fanhao Shen,[2] Feitong Jin,[2] Xuhao Zhu,[2] Yujie Ji,[2] Shibo Xu,[2] Jiachen Chen,[2] Yaozu Wu,[2] Chuanyu Zhang,[2] Yu Gao,[2] Ning Wang,[2] Yiren Zou,[2] Aosai Zhang,[2] Tingting Li,[2] Zehang Bao,[2] Zitian Zhu,[2] Jiarun Zhong,[2] Zhengyi Cui,[2] Yihang Han,[2] Yiyang He,[2] Han Wang,[2] Jianan Yang,[2] Yanzhe Wang,[2] Jiayuan Shen,[2] Gongyu Liu,[2] Zixuan Song,[2] Jinfeng Deng,[2] Hang Dong,[2] Pengfei Zhang,[2] Shao-Kai Jian,[4] Hekang Li,[2] Zhen Wang,[2,5] Junxiang Zhang,[2] Qiujiang Guo,[2,5] Hai-Qing Lin,[3] Chao Song,[2,5,†] Xue-Jia Yu,[6,7,‡] H. Wang,[2,5,§] and Fei Wu[1]

[1]*College of Computer Science and Technology, Zhejiang University, Hangzhou 310027, China*
[2]*School of Physics, ZJU-Hangzhou Global Scientific and Technological Innovation Center, and Zhejiang Key Laboratory of Micro-nano Quantum Chips and Quantum Control, Zhejiang University, Hangzhou 310000, China*
[3]*Institute for Advanced Study in Physics and School of Physics, Zhejiang University, Hangzhou 310058, China*
[4]*Department of Physics and Engineering Physics, Tulane University, New Orleans, Louisiana, 70118, USA*
[5]*Hefei National Laboratory, Hefei 230088, China*
[6]*Department of Physics, Fuzhou University, Fuzhou 350116, Fujian, China*
[7]*Fujian Key Laboratory of Quantum Information and Quantum Optics, College of Physics and Information Engineering, Fuzhou University, Fuzhou, Fujian 350108, China*

* These authors contributed equally
† chaosong@zju.edu.cn
‡ xuejiayu@fzu.edu.cn
§ hhwang@zju.edu.cn

I. THEORETICAL UNDERSTANDING

A. Introduction to the gapless symmetry-protected topological phases

To provide a more intuitive understanding of symmetry-protected topological properties in critical systems, we first introduce the fundamental concepts of gapless symmetry-protected topological phases (gSPTs). In this work, we study a prototypical model called the critical cluster Ising model in experiments as a concrete example.

Topological phases form a cornerstone of modern condensed matter physics, extending beyond the Landau-Ginzburg-Wilson paradigm of symmetry-breaking. A notable example of topological states is symmetry-protected topological phases [1–3], which are typically associated with a bulk energy gap. It has been widely believed that these topological properties are destroyed when the bulk gap closes. However, recent achievements [4–8] have shown that many key features of topological physics, such as topological edge modes, can surprisingly emerge in the less explored realm of gapless quantum many-body systems. These systems include stable gapless phases or critical points, leading to the notion of gSPT phases. The topologically nontrivial quantum critical point (or state) discussed in the main text represents a special type of gSPT.

To date, different families of gSPTs have been identified in the literature [9–12], and the classification of these phases based on whether they contain gapped sector and whether they are intrinsic (a term that will be clarified below), thereby leading to the categorization into four distinct types, as summarized in Table S1. The subsequent detailed explanations are mainly based on the literature [9].

	Contains gapped sector	No gapped sector
Non-intrinsic	gSPT	purely gSPT
Intrinsic	igSPT	intrinsically purely gSPT

TABLE S1. Classification of the gSPTs by whether they are purely gapless (horizontal direction) or intrinsically gapless (vertical direction). The table is taken from Ref. [9].

i) *The gSPT phases*: The first example of a gSPT phase, which is non-intrinsic (which means such topological phases has gapped counterparts) and includes a gapped sector, was systematically investigated in Ref. [4]. Specifically, a general construction of gSPT phases was introduced based on the decorated domain-wall (defect) picture of gapped SPT phases [13]. The central idea is to decorate the G-symmetry defects of a G-symmetric gapless system or conformal field theory (CFT) with an H-symmetric gapped SPT. This decorated defect construction creates a gapped sector that acts both on G and H symmetry, resulting in a gSPT phase whose topological properties can also manifest in gapped counterparts. As a result, these features are not "intrinsic" to the gapless system [4, 12]. In summary, the topological properties of these gSPT phases arise from the gapped SPT sector and can be interpreted as a gapped SPT stack with a CFT. Recent studies [6] have shown that such gSPT states can emerge at conformally invariant critical points separating spontaneously symmetry-breaking (SSB) phases and gapped SPT phases, also known as symmetry-enriched CFT or topologically nontrivial quantum critical points [6].

ii) *The intrinsically gSPT phases*: On a different front, there exists an intriguing class of gapless topological phases, referred to as intrinsically gSPT (igSPT) phases [14], whose topological features are fundamentally prohibited in gapped counterparts. Specifically, recent works [9, 12] propose a systematic construction of igSPT phases, which we briefly outlined below: The total symmetry group is denoted by Γ, fitting into the group extension $1 \to H \to \Gamma \to G \to 1$. The construction begins with a G-symmetric gapless system or CFT characterized by a self-anomaly ω_G. An H-symmetric gapped SPT phase is then stacked on top of the G symmetry domain walls (defects). Due to the non-trivial group extension, the resulting gapped sector exhibits an (emergent) anomaly $-\omega_G$ that cancels the anomaly in the gapless sector, rendering the combined system an igSPT phase that is Γ-anomaly-free. By construction, igSPT phases also include a gapped sector, leading to exponentially localized edge modes near the boundaries. Importantly, the topological features of igSPT phases cannot be realized in any Γ-symmetric gapped SPT phase, thereby justifying the term "intrinsic". Furthermore, Li et al. [9, 12] utilized the decorated defect construction and the Kennedy-Tasaki (KT) transformation to construct analytically tractable 1+1D spin models of both gSPT and igSPT phases, focusing on $\mathbb{Z}_2 \times \mathbb{Z}_2$ symmetry and $\mathbb{Z}_4$ symmetry, respectively. Additionally, the recently developed topological holography principle (known as symmetry topological field theory) was employed to provide a unified classification of gapped and gapless SPT phases from a new perspective [10, 15]. Experimentally, these igSPT phases can emerge at the transition point between a quantum spin Hall insulator and an s-wave superconducting phase, which has recently been proposed to be realizable in materials such as WTe_2 [16].

iii) *The purely and intrinsically purely gSPT phases*: From the previous discussion, we have established that both gSPT and igSPT phases typically include a gapped sector, which results in exponentially localized topological edge modes. However, Verresen et al.[6, 17] studied the critical cluster Ising model with time-reversal symmetry and demonstrated that this model lacks a gapped sector, as evidenced by the algebraically decaying energy splitting of edge modes that are forbidden in gapped systems. This result suggests the existence of a gSPT phase without any gapped sector, referred to as a "purely gSPT phase" [9–12]. However, to the best of our knowledge, the ground state of the critical cluster Ising chain provides the only known example of

a purely gSPT phase. Therefore, constructing additional lattice Hamiltonians that realize such novel phases is highly desirable. Furthermore, it is natural to explore the possibility of an igSPT phase without any gapped sectors, which has been termed an "intrinsically purely gapless SPT phase" [9]. Unfortunately, despite ongoing efforts [9], constructing such an intrinsically purely gSPT phase remains an open challenge, leaving it as an important direction for future research.

It is important to emphasize that, although a topological semimetal can be broadly considered a gapless SPT phase, there is a qualitative distinction between their topological properties: the former relies on space-translational symmetry, making it susceptible to destabilization by disorder. In contrast, the topological edge modes at quantum criticality remain robust even in the presence of symmetry-preserving disorder.

To provide a concrete and experimentally accessible example, we consider the following prototypical lattice Hamiltonian, previously studied in Ref. [18, 19], as an example of a purely gSPT phase:

$$H = -\sum_i JZ_{i-1}X_iZ_{i+1} - \sum_i gZ_iZ_{i+1} - \sum_i hX_i\,, \tag{1}$$

where X, Y, Z denote the Pauli matrices. The model enjoys the $\mathbb{Z}_2$ spin-flip symmetry (generated by $P = \prod_i X_i$) and the time-reversal symmetry $\mathbb{Z}_2^T$ (acting as the complex conjugation). The parameters g, h, J represent ferromagnetic (FM) coupling, transverse field, and cluster interactions, respectively, which drive the system toward FM, trivial paramagnetic (PM), and $\mathbb{Z}_2 \times \mathbb{Z}_2^T$ SPT [17, 20] phases, respectively. When $h = 0, g = 1$, the model reduces to the cluster Ising model discussed in the main text.

We notice that although the FM-PM ($J = 0, g = h$) and FM-SPT ($h = 0, J = g$) transitions are both described by the 1+1D Ising CFT, the time-reversal symmetry acts differently on the disorder operator, leading to different symmetry-enriched CFTs [6]. We refer to the former as the topologically trivial and the latter as the topologically nontrivial Ising critical point (purely gSPT phase). To briefly explain why this topological distinction arises, we note that both Ising critical points have a unique local (nonlocal) scaling operator with scaling dimension $\Delta = 1/8$, typically denoted by σ (μ). These serve as the order parameters of the adjacent phases: $\sigma(i) \sim Z_i$ is the Ising order parameter that characterizes the FM order phase, while the disorder operator $\mu(i)$ is the Kramers-Wannier-dual string order parameter that characterizes the symmetry-preserving phase (trivial PM and cluster SPT phases). In the trivial PM phase, $\mu(i) \sim \prod_{j=-\infty}^{i} X_j$, while in the cluster SPT phase, $\mu(i) \sim (\prod_{j=-\infty}^{i-1} X_j)Y_iZ_{i+1}$ [17]. The distinction is reflected in the symmetry charge of the disorder operator under time-reversal symmetry: $T\mu T = \pm\mu$, which means that the two critical points can not be smoothly connected and must be separated by another phase transition. In the non-trivial case ($T\mu T = -\mu$), a topologically protected edge mode persists even when the bulk gap closes [6]. Intuitively, the boundary of such a critical system spontaneously breaks the $\mathbb{Z}_2$ spin-flip symmetry, resulting in a two-fold degenerate edge mode that is stable because the charged μ operator cannot condense near the boundary. The finite-size splitting of this edge mode decays algebraically as $\sim 1/L^{14}$, which is parametrically faster than the finite-size bulk gap $\sim 1/L$. This faster decay ensures the stability of the topological edge mode, even in the presence of critical bulk fluctuations. In essence, the topologically distinct Ising critical points realize different conformal boundary conditions and boundary g-functions at low energy, serving as a form of "generalized ground-state degeneracy" even for gapless topological phases without edge modes [7]. The most important aspects of gSPT phases are the topological invariants, distinguishing different gSPT phases, and the bulk-boundary correspondence, a universal feature of gSPT phases. Fortunately, in a critical system described by CFT, these two aspects are reflected in the **boundary g-function** and the **bulk entanglement spectrum**, respectively. These quantities are the main focus of our experiment and are typically extrapolated using the critical ground state in theoretical treatment. However, in this work, we investigate whether the more experimentally accessible low-lying critical states can effectively capture the fundamental quantities of gSPT phases.

B. The boundary g-function serves as a topological invariant for classifying topologically distinct quantum critical states

Traditionally, people are often interested in the low-energy universal behavior of critical many-body systems in the thermodynamic limit, known as the universality class or more specifically, the bulk universality class. This is typically described by the (bulk) CFT. A key quantity in determining such bulk critical universality is the central charge, which can be extracted from the entanglement entropy of a subsystem of length l under periodic boundary conditions (PBCs) (e.g., for a one-dimension critical spin chain of total size L):

$$S^{\mathrm{PBC}}(L, l) = \frac{c}{3}\ln\left(\frac{L}{\pi}\sin\left[\frac{\pi l}{L}\right]\right) + c_1^{\mathrm{PBC}}\,, \tag{2}$$

where c_1^{PBC} is a non-universal constant, and c is the central charge of the underlying CFT. The central charge serves as a fingerprint for classifying the bulk universality class of quantum phase transitions and has garnered extensive theoretical and experimental attention [21, 22].

However, in the presence of a boundary, an intriguing degree of freedom emerges where the bulk of the system can remain at a critical point, while the boundary may flow between different fixed points under boundary renormalization group transformations. The universal behavior of a critical system with a boundary, referred to as boundary (or surface) criticality, exhibits richer physics

compared to bulk universality and can be effectively characterized using boundary CFT [23]. According to the observation in Ref. [24], for a system with its bulk at the critical point, one can define an Affleck-Ludwig boundary entropy. This boundary entropy decreases under boundary renormalization group flow and equals to a number which is related to the universality class of the corresponding conformal boundary condition at the boundary fixed point. These boundary critical phenomena were first discussed in detail in the 1970s and have recently gained renewed attention due to their relevance in many areas of modern physics [25, 26]. In particular, in the context of gSPT phases or topologically nontrivial quantum critical points, recent advances [7] have unambiguously demonstrated that conformal boundary conditions (or equivalently, the boundary g-function) can serve as a topological invariant for topologically nontrivial conformal critical points, at least in 1+1D, encoding nontrivial topological properties that go beyond topological edge modes. The boundary entropy can be explicitly defined in terms of entanglement entropy under certain boundary conditions, using a one-dimensional critical spin chain with boundary b as an example:

$$S^{\mathrm{b}}(L,l) = \frac{c}{6}\ln\left(\frac{2L}{\pi}\sin\left[\frac{\pi l}{L}\right]\right) + \frac{c_1^{\mathrm{PBC}}}{2} + \ln g + \mathbb{G}_b(l/L)\,, \tag{3}$$

where g is the boundary g-function, which fully determines the boundary universality class and plays a role analogous to the central charge for bulk universality. The term $\mathbb{G}_b$ represents a scaling function, which is generally challenging to determine analytically. Consequently, extracting the boundary g-function from the entanglement entropy is typically difficult, particularly in experimental settings where scalable measurements are even more challenging to achieve. To avoid potential confusion, we emphasize the distinction between two types of boundary conditions discussed throughout this paper: **physical boundary conditions** and **conformal boundary conditions**. The physical boundary condition refers to specific operations imposed on the boundary of the ultraviolet (or microscopic) lattice system, and we refer to it in the main text simply as "boundary condition". In contrast, the conformal boundary condition corresponds to the boundary fixed point that emerges under the boundary renormalization group flow in the infrared limit. Importantly, these two types of boundary conditions are generally not directly related.

C. Extract the boundary g-function from the wavefunction overlaps

To address the scaling challenges associated with entanglement entropy to extract the boundary g-function, recent theoretical progress [27, 28] have introduced a wavefunction overlap method. This approach offers a direct means to determine the value of the boundary g-function, eliminating the need to extract it indirectly through fitting the entanglement entropy. Thanks to the operator-state correspondence in CFT, expressions in terms of primary operators can be translated into the form involving the corresponding states. More specifically, as proofed in Ref. [28], the overlap between two low-lying eigenstates of the Hamiltonian with different defect deformations can be related to universal defect data, such as the defect g-function, the scaling dimension of the defect change operator Δ_α^{ab}, and the four-point correlation function for defect change operators. Finally, by choosing suitable eigenstates, the universal data can be extracted from the ratio of different wavefunction overlaps by canceling out the unwanted parts. In particular, the g-function can be obtained by taking the ratio

$$g_a^{\mathrm{Def}} = \left(\frac{\langle\phi_0^{00}|\phi_0^{a0}\rangle}{\langle\phi_0^{aa}|\phi_0^{a0}\rangle}\right)^2, \tag{4}$$

where $|\phi_\alpha^{ab}\rangle$ is the eigenstate of the Hamiltonian with defect deformations

$$H^{ab} = H + \lambda O^a_{L-1,0} + \lambda' O^b_{L/2-1,L/2}\,, \tag{5}$$

which corresponds to the primary operator ϕ_α^{ab}. The superscript a denotes the defect type ($a = 0$ means the trivial defect) while the subscript α labels the primary operator ($\alpha = 0$ means the lowest primary operator corresponding to the ground state of the defect Hamiltonian) and the perturbation $O^a_{j,j+1}$ is the lattice realization of the defect type a at sites j and $j+1$.

It is noted that the g-function, g_a^{Def}, in Eq. (4) is the defect g-function. Actually, the boundary is a special type of line defect and the boundary g-function is the square root of its defect correspondence [29]. In the following, we use g_a to denote the boundary g-function for the boundary condition a and the square in Eq. (4) should be removed in its calculations.

At last, we note that the expression Eq. (4) can be generalized to low-lying excited states corresponding to defect primary operators and the ratio of the wavefunction overlaps is

$$\frac{\langle\phi_\beta^{00}|\phi_\alpha^{a0}\rangle}{\langle\phi_\gamma^{aa}|\phi_\delta^{a0}\rangle} = g_a\frac{C^{0a0}_{0\alpha\beta}}{C^{a0a}_{\delta 0\gamma}}\,, \tag{6}$$

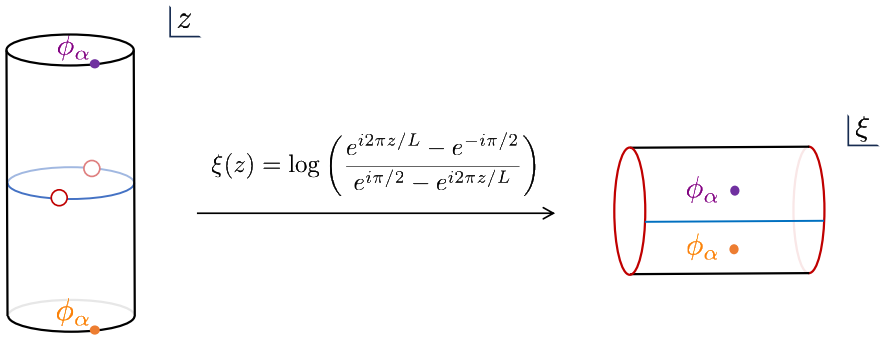

FIG. S1. **Explanation for the double degenerate of the entanglement spectrum calculated from the low-lying quantum critical state.** The red circle represents the UV cutoff induced by the entanglement cut and ϕ_α is the primary operator inserted at the infinity past/future imaginary time, which corresponds to the eigenstate $|\phi_\alpha\rangle$ of the periodic Hamiltonian. Via the conformal mapping $\xi(z)$, the primary operators are mapped into local operators in the bulk, which does not influence the boundary in the imaginary-time evolution.

where $C^{0a0}_{0\alpha\beta}$ and $C^{a0a}_{\delta 0\gamma}$ are defect operator product expansion (OPE) coefficients. It means that the ratio of overlaps between different excited states is proportional to the boundary g-function, with the proportionality constant determined by the ratio of the corresponding OPE coefficients. In principle, if the OPE coefficients of the underlying CFT are known, the boundary g-function can be extracted using the wavefunction overlap method, even for excited states. In our experiments, which corresponds to the Ising CFT, the $\mathbb{Z}_2$-odd sector σ under the periodic boundary condition is projected out as part of an error mitigation strategy because the correct ground state is in the $\mathbb{Z}_2$-even sector. Under this condition, the ratio between the relevant OPE coefficients all equal to 1 [27], leading to a direct equivalence between the wavefunction overlap of low-lying excited states and the boundary g-function. This simple argument provides an intuitive explanation for why an accurate boundary g-function can be obtained from low-lying critical states. A more detailed and systematic investigation of this significant and intriguing question for general cases is left for future work.

D. Universal entanglement spectrum at topologically nontrivial critical states

The concept of the entanglement spectrum is a powerful tool in the study of topological phases of matter and SPT physics. As first noticed by Li and Haldane in their seminal work [30], the entanglement spectrum of a reduced density matrix is believed to encode additional information on the existence of the degenerate edge modes at the boundary of a gapped topological phase, which cannot be captured by the entanglement entropy. However, a remaining question is wether this observation still holds in gapless topological phases. This question has been addressed in a recent work [8, 31], at least in the context of one-dimensional gapless SPTs. Through extensive numerical calculations and conformal mappings, it has been found that the entanglement spectrum not only captures the topological edge degeneracy but also the operator content of the boundary CFT. Therefore, to experimentally observe the nontrivial edge degeneracy of the critical cluster-Ising chain, one can probe the entanglement spectrum of a contiguous interval of the periodic critical chain; the two-fold degeneracy in the low-lying entanglement spectrum reflects the nontrivial edge states. In this work, the bulk entanglement spectrum is obtained from the prepared state via the Entanglement Hamiltonian Tomograph (EHT) method, which can be performed efficiently on digital quantum simulation platforms.

To provide an intuitive explanation for why the low-lying quantum critical state generated in experiments can effectively exhibit topological degeneracy in the bulk entanglement spectrum, we begin with the state-operator correspondence in CFT. According to this principle, a low-lying excited state can be interpreted as an operator inserted at infinity, as illustrated in Fig. S1. By applying a series of conformal transformations, the reduced density matrix of the low-lying quantum critical state can be mapped onto a cylinder. In this context, the excited states correspond to bulk local operators ϕ_α in imaginary time. However, the critical cluster Ising model is known to host two decoupled fractionalized edge states in the Majorana representation [5]. Consequently, the imaginary-time evolution of the bulk local operator does not influence the edge states, thereby preserving the double degeneracy in the entanglement spectrum. The more detailed proof for general cases can be left as future work.

II. DETAILS OF THE DENSITY MATRIX RENORMALIZATION GROUP METHOD

To better understand the prepared state, we need to analyze its overlap with the low-lying excited states of the target many-body Hamiltonian. For this purpose, we employ the Density Matrix Renormalization Group (DMRG) method [32] based on the Matrix

Product State (MPS) [33] formalism to solve the first several low-lying eigenstates of the cluster-Ising model under different boundary conditions.

By exploiting the MPS representation, a quantum state can be expressed in a compact form:

$$|\psi\rangle = \sum_{\{\sigma_i\}} M^{\sigma_1}_{1,a_1} \cdots M^{\sigma_i}_{a_{i-1},a_i} \cdots M^{\sigma_L}_{a_{L-1},1} |\sigma_1 \cdots \sigma_L\rangle \ , \tag{7}$$

where $\sigma_i = \uparrow, \downarrow$ is a local basis of the qubit on site i, and M^{σ_i} are matrices with appropriate dimensions so that their multiplication leads to a scalar, namely, the wavefunction $\langle\sigma_1 \cdots \sigma_L|\psi\rangle$. The ground state of the Hamiltonian can be obtained by optimizing the local matrices according to the variational principle. Once the expectation value of the Hamiltonian with respect to the MPS has reached the convergence criterion, the optimization process would stop and the final MPS can be used to represent the true ground state faithfully. The dimension of the bond index $\dim(a_i)$ is a tunable parameter called bond dimension which controls the representation ability of the MPS. In practical simulations, we have chosen a sufficiently large bond dimension up to 1024 to ensure the accuracy of the optimized MPS.

To access the excited eigenstates, we adopt a standard strategy by introducing an energy penalty for all the already obtained eigenstates. Assume that we have calculated the first m low-lying eigenstates $\{|\psi_k\rangle\}_{k=1}^m$ of the Hamiltonian, to obtain the $(m+1)$th eigenstate, we consider a modified Hamiltonian:

$$H_{m+1} = H + \lambda \sum_{k=1}^{m} |\psi_k\rangle\langle\psi_k| \ , \tag{8}$$

where λ is the penalty strength which should be large enough to shift the energies of the first m eigenstates higher than the energy of the $(m+1)$th eigenstate ($\lambda = 50$ in our work). Based on the modified Hamiltonian H_{m+1}, the $(m+1)$th eigenstate of H can be accessed by running a conventional DMRG calculation. In this way, the first several low-lying excited states of the Hamiltonian can be systematically computed one by one.

In the present work, the DMRG and MPS simulations are performed via ITensor [34] and Quimb [35] packages.

III. EXPERIMENTAL DETAILS

A. Further Simulations

We devise an efficient state preparation algorithm for the cluster Ising model that prioritizes maximizing the overlap with the ground state. We then introduce a symmetry projection method to extract the boundary g-function and utilize entanglement Hamiltonian tomography to probe the two-fold degeneracy of the entanglement spectrum. In this paper, quantum circuit simulations of small system sizes ($L \leq 20$) are performed via a state vector simulator from Pennylane [36] with Pytorch [37] backend and simulations of large system sizes ($L > 20$) are performed via an MPS simulator from Tensorcircuit [38] with Tensorflow [39] backend.

A optimization workflow for entanglement Hamiltonian tomography is illustrated in Fig S4.

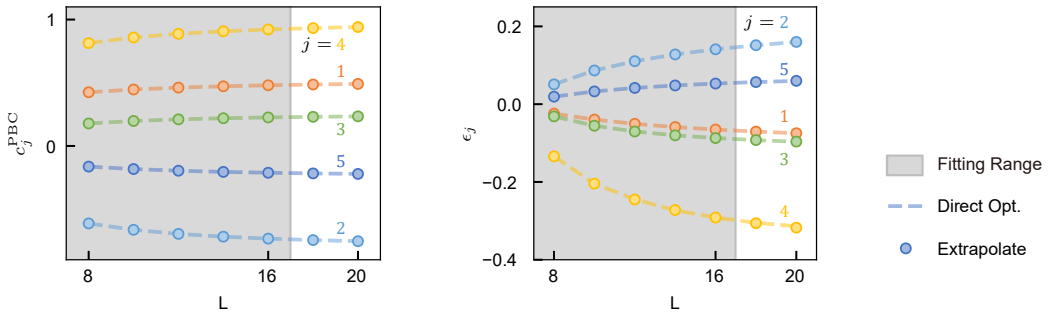

FIG. S2. **Verification of the extrapolating functions.** The dotted lines indicate parameters optimized directly without using energy-initialized parameters. Markers indicate the fitted and extrapolated parameters.

We optimized the parameters by maximizing the fidelities with the target states using systems of up to 16 qubits, from which we fitted the extrapolation functions. We further optimize the circuit parameters $(\epsilon_j, c_j^{\mathrm{PBC}})$ directly for $L = 18$ and $L = 20$ and

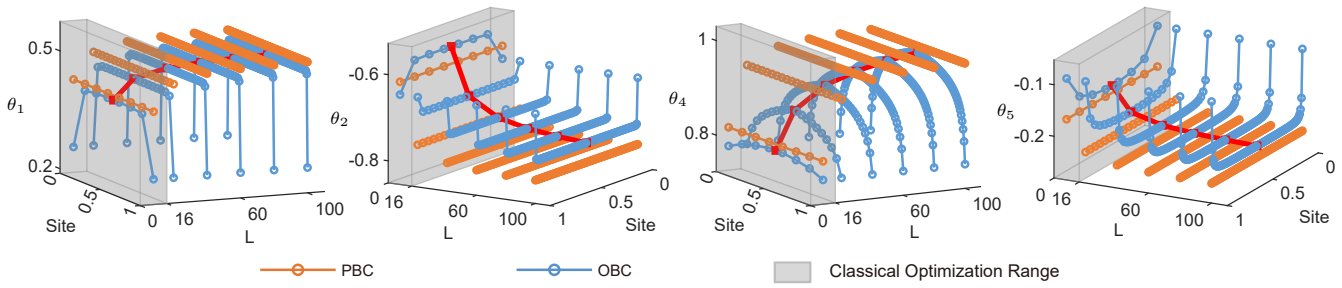

FIG. S3. **Single-qubit rotation angles for other layers of the circuit.**

block index(j)	1	2	3	4	5
$b_j(\epsilon_j)$	-0.930	-0.710	-1.479	-0.813	-0.766
$b_j(c_j^{\mathrm{PBC}})$	-1.365	-1.892	-1.780	-1.651	-1.894

TABLE S2. **Optimized b_j in the extrapolation function of all five blocks**. The negative nature converges the single-qubit gate rotation angles to the infinite-volume ($L \to \infty$) limit in a power-law speed.

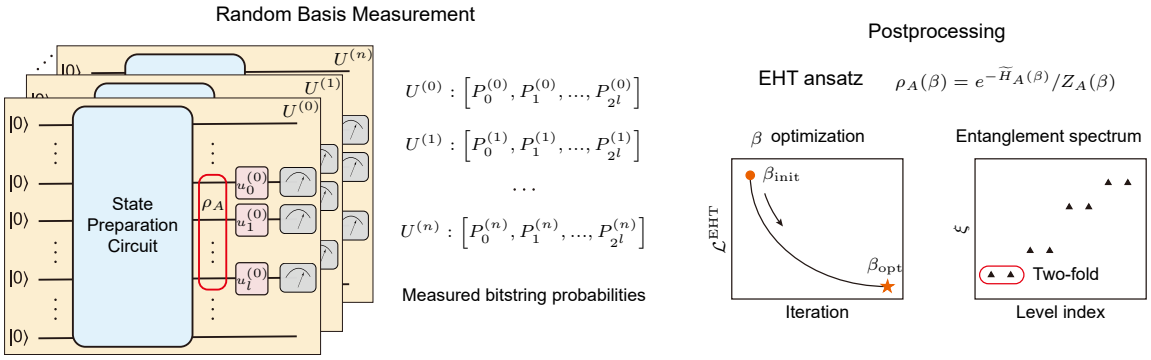

FIG. S4. **EHT optimization workflow.** We first measure bitstring probabilities of the prepared PBC state under different Pauli bases. Then we fit β in the EHT ansatz to the measured data. With the optimized β, we calculate the subsystem's entanglement spectrum and observe a two-fold topological degeneracy.

observe a good agreement with the extrapolated ones. The resulting parameters of the third circuit block for OBC and PBC are displayed in Fig. 2**b** in the main text, and the parameters of the left circuit blocks are shown in Fig. S3. b_js for both ϵ_j and c_j^{PBC} in the extrapolation function are negative as shown in Table S2.

B. Device Information

The experiment is performed on a superconducting quantum chip containing 125 qubits and 218 couplers, from which spin chains with various sizes can be constructed, as illustrated in Fig. S5.

The qubits have a mean energy relaxation time T_1 of 64.6 μs and dephasing time (obtained by spin Echo) T_2 of 19.1 μs, which are measured at the qubit idling frequencies. The single- and two-qubit gates are implemented following the procedure outlined in [40], with gate lengths of 20 and 32 ns, respectively. The qubit measurements are optimized using the method described in [41]. The distributions of gate and measurement error rates are presented in Fig. S6, with dashed lines indicating the median values. Single- and two-qubit gate errors are estimated with simultaneous cross-entropy benchmarking technique.

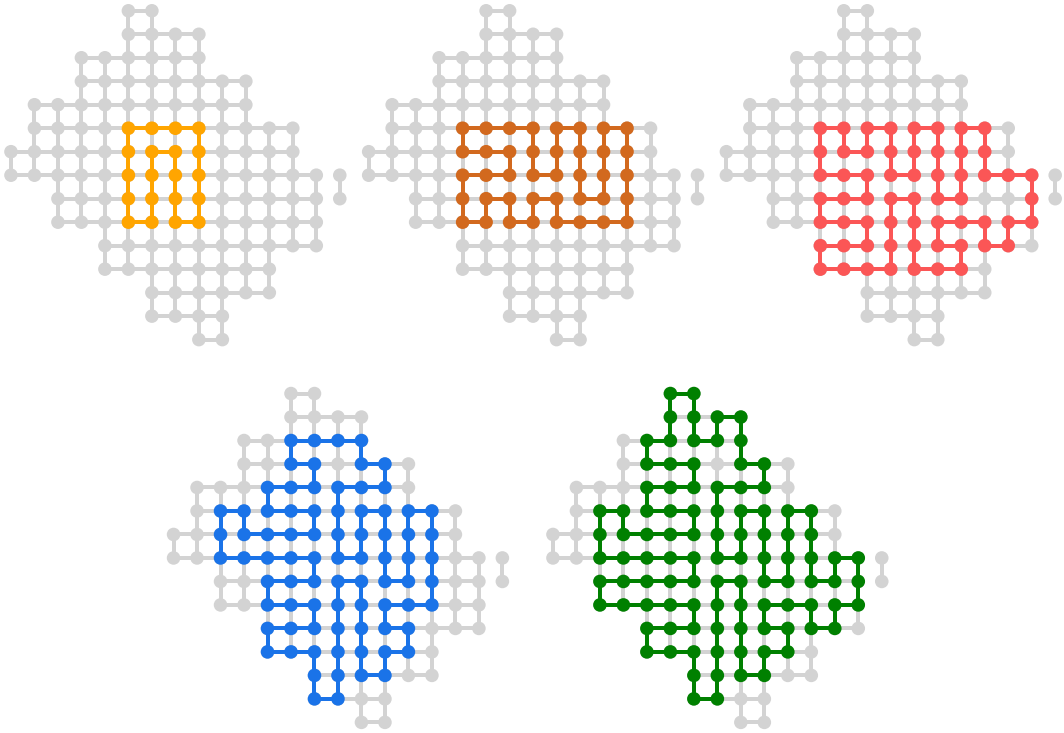

FIG. S5. **Qubit layout details.** We construct 1D qubit chains with 20, 40, 60, 80, and 100 qubits out of the 125-qubit superconducting processor.

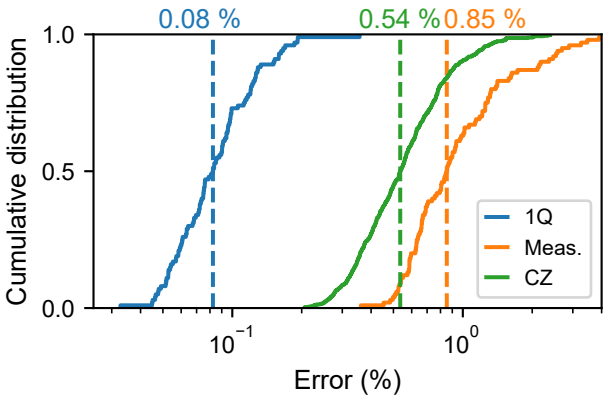

FIG. S6. **Cumulative distributions of gate Pauli errors and measurement error.** The dashed lines indicate the median values. We consider every CZ gate used in our experiments into the distribution, with some couplers used multiple times. The measurement error is calculated from the average error of $|0\rangle$ and $|1\rangle$.

C. Error Mitigation

In this part, we outline the error mitigation strategies employed in our experiments. Specifically, we combine Zero Noise Extrapolation (ZNE) with Pauli twirling (PT) and circuit simplification for energy measurements and use PT and circuit simplification for boundary g-function measurements.

1. Zero Noise Extrapolation

To mitigate the effects of noise in the quantum circuits, we apply Zero Noise Extrapolation (ZNE) in conjunction with random Pauli twirls. We estimate the error-free outcome by running unitary-equivalent quantum circuits at different noise levels. Due to the regular structure of our state preparation circuit, it is particularly well-suited for applying ZNE with unitary folding [42], which increases the noise level of the circuit. We implement Pauli twirling (PT) at each noise level to transfer the coherent errors into Pauli errors, which involves randomly applying a sequence of Pauli operations to the quantum system and averaging the results over multiple randomized circuits. We observe that the averaged outcomes become stable when the number of random Pauli-twirled circuits reaches 25. We then extrapolate the circuit's outcome as the noise approaches zero with a linear model. This enables us to estimate the ideal, noise-free results.

In Fig. S7, we present the results of the energy measurement experiment and the error-mitigated outcomes for the 100-qubit PBC ground state. The experimental state preparation circuit consists of 4 CZ gate layers and 5 single-qubit gate layers. To increase the noise levels, we randomly select and fold different numbers of CZ gate layers as well as the adjacent single-qubit gate layers. For example, the noise scale factor would be three if we fold each CZ layer exactly once. The error bars are computed using bootstrapping, where we resample shots uniformly with replacements from the pool of shots for all 25 Pauli-twirled circuits. This procedure generates 100 mitigated energy expectation values, from which we calculate the mean and standard deviation.

We tried to use both linear and exponential extrapolation to extract the error-mitigated value. While the exponential extrapolation could sometimes yield outcomes with less errors, we found a larger deviation compared with the results obtained based on linear extrapolation. Besides, we also observed that the exponential model is less stable than the linear model. Therefore, we adopted linear extrapolation in our experiment.

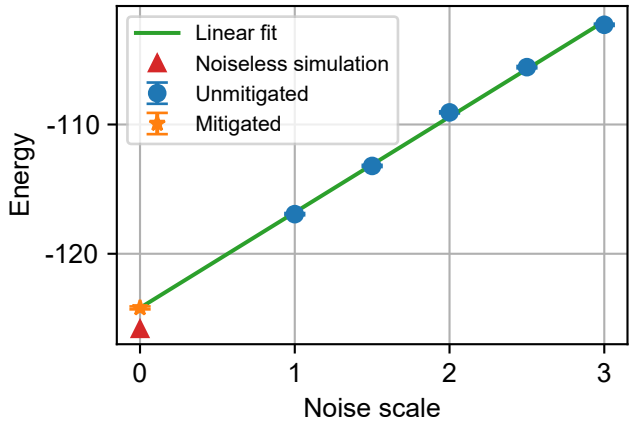

FIG. S7. **Energy measurement with zero noise extrapolation.** We display the measured energies of a 100-qubit PBC ground state with different noise scale factors ($F \in \{1, 1.5, 2, 2.5, 3\}$). For each noise scale, we add Pauli twirls in 25 randomly folded circuits. Error bars indicate 68% confidence interval, obtained from bootstrapping 100 configurations.

2. Circuit Simplification

During the measurement of state energies and overlaps, the circuit can be further simplified according to the commutation relations between CZ gates and single-qubit Pauli operators, as depicted in Fig. S8.

Specifically, rewriting the unitary of the state preparation circuit as $U = U_{\mathrm{CZ}}U'$, where U_{CZ} represents the unitary of the last CZ layer, and U' denotes the circuit unitary excluding the last CZ layer, we have $|\Psi\rangle = U_{\mathrm{CZ}}U'|0\rangle^{\otimes L}$. The expectation value of an observable O can be written as

$$\langle\Psi|O|\Psi\rangle = \langle 0|^{\otimes L}U'^{\dagger}U_{\mathrm{CZ}}OU_{\mathrm{CZ}}U'|0\rangle^{\otimes L} = \langle 0|^{\otimes L}U'^{\dagger}O'U'|0\rangle^{\otimes L}, \tag{9}$$

where $O' = U_{\mathrm{CZ}}OU_{\mathrm{CZ}}$. Since the observable O in our experiment is a Pauli operator, O' remains a Pauli operator, enabling the removing of CZ layer by substituting O.

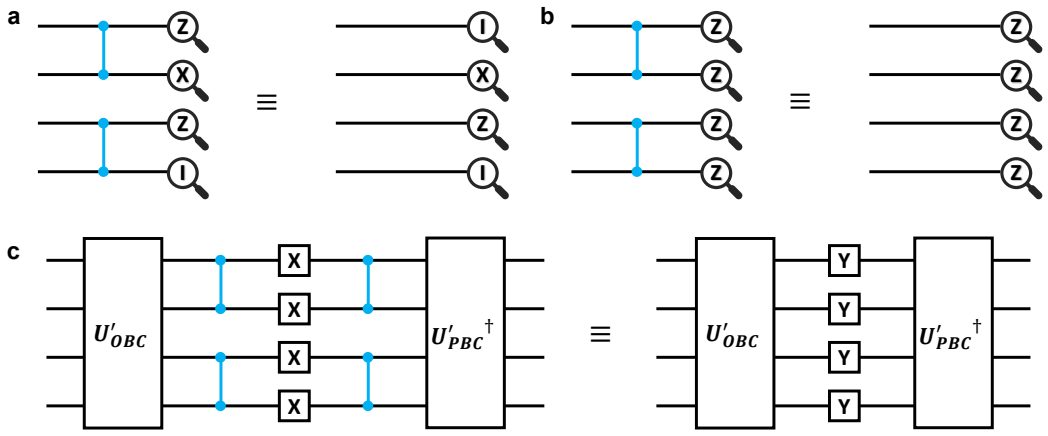

FIG. S8. **Circuit simplification for energy and overlap measurement. a** and **b**, In the energy measurement circuit, the final CZ gate layer is eliminated by modifying the observables according to Eq. 9. **c**, In the overlap measurement circuit, the Pauli X gates, which are sandwiched between two CZ gate layers in the middle of the circuit, can be simplified to a single layer of Pauli Y gates.

3. *Intrinsic Noise Resistance*

The boundary g-function measurement and EHT-based entanglement spectrum detection are naturally resistant to noise. For the boundary g-function, both the numerator and denominator overlaps will decrease under decoherent noise, but their ratio remains nearly constant. In Fig. S9, We simulate the effect of CZ depolarization error on the measurement of boundary g-function for a system size $L = 8$, and observe that the resulting g-function remains robust over a wide range of noise rates.

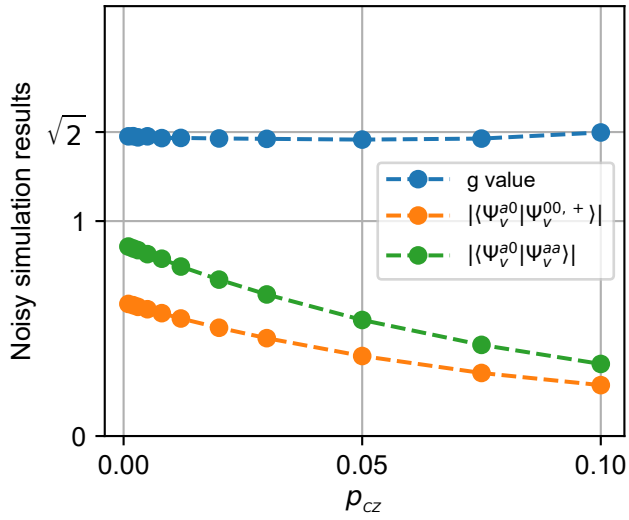

FIG. S9. **Robustness of g-function measurement.** We perform noisy circuit simulations on 8 qubits with experimentally measured T_1 and T_2. We add an additional CZ depolarization channel with controlled depolarizing rate, denoted by p_{CZ}. While the overlap decreases as the depolarizing rate increases, the g-function value remains almost unaffected, demonstrating its robustness.

To demonstrate the robustness of EHT to noises, we first extract the noiseless density matrix ρ of an eight-qubit subsystem from the 100-qubit ground state with PBC, which is obtained using DMRG. We then introduce a depolarizing channel to the system, obtaining the noisy density matrix $\rho_n = (1-p)\rho + pI/d$, where p is the depolarizing error rate and $d = 2^8$. As shown in Fig. S10, the fidelity between ρ and ρ_n decreases with the increase of the depolarizing error rate as expected. In contrast, when we apply EHT on the eight qubits with the loss function defined in Eq. 4 in the main text and random 200 Pauli bases, we find

that the fidelities of the resulting density matrices ρ_{EHT} to ρ are much less affected by the depolarizing noises.

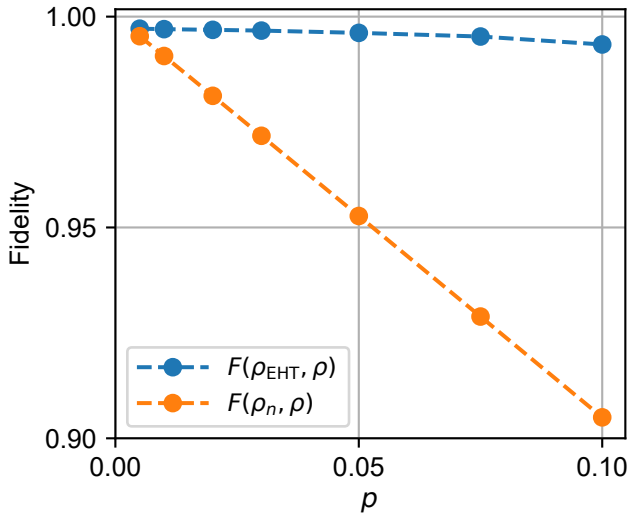

FIG. S10. **EHT noisy simulation.** We compare the fidelity between ρ and ρ_{EHT} , as well as ρ_n with different depolarizing rate p. The results demonstrate that the EHT learning protocol is robust to depolarizing noise.

[1] X.-G. Wen, Rev. Mod. Phys. **89**, 041004 (2017).
[2] X.-L. Qi and S.-C. Zhang, Rev. Mod. Phys. **83**, 1057 (2011).
[3] M. Z. Hasan and C. L. Kane, Rev. Mod. Phys. **82**, 3045 (2010).
[4] T. Scaffidi, D. E. Parker, and R. Vasseur, Phys. Rev. X **7**, 041048 (2017).
[5] R. Verresen, N. G. Jones, and F. Pollmann, Phys. Rev. Lett. **120**, 057001 (2018).
[6] R. Verresen, R. Thorngren, N. G. Jones, and F. Pollmann, Phys. Rev. X **11**, 041059 (2021).
[7] X.-J. Yu, R.-Z. Huang, H.-H. Song, L. Xu, C. Ding, and L. Zhang, Phys. Rev. Lett. **129**, 210601 (2022).
[8] X.-J. Yu, S. Yang, H.-Q. Lin, and S.-K. Jian, Phys. Rev. Lett. **133**, 026601 (2024).
[9] L. Li, M. Oshikawa, and Y. Zheng, "Intrinsically/purely gapless-spt from non-invertible duality transformations," (2023), arXiv:2307.04788 [cond-mat.str-el].
[10] R. Wen and A. C. Potter, "Classification of 1+1d gapless symmetry protected phases via topological holography," (2023), arXiv:2311.00050 [cond-mat.str-el].
[11] R. Wen and A. C. Potter, Phys. Rev. B **107**, 245127 (2023).
[12] L. Li, M. Oshikawa, and Y. Zheng, SciPost Phys. **17**, 013 (2024).
[13] X. Chen, Y.-M. Lu, and A. Vishwanath, Nature communications **5**, 3507 (2014).
[14] R. Thorngren, A. Vishwanath, and R. Verresen, Phys. Rev. B **104**, 075132 (2021).
[15] S.-J. Huang and M. Cheng, "Topological holography, quantum criticality, and boundary states," (2023), arXiv:2310.16878 [cond-mat.str-el].
[16] T. Song, Y. Jia, G. Yu, , *et al.*, Nature Physics **20**, 269 (2024).
[17] R. Verresen, R. Moessner, and F. Pollmann, Phys. Rev. B **96**, 165124 (2017).
[18] C. M. Duque, H.-Y. Hu, Y.-Z. You, V. Khemani, R. Verresen, and R. Vasseur, Phys. Rev. B **103**, L100207 (2021).
[19] X.-J. Yu and W.-L. Li, Phys. Rev. B **110**, 045119 (2024).
[20] W. Son, L. Amico, R. Fazio, A. Hamma, S. Pascazio, and V. Vedral, Europhysics Letters **95**, 50001 (2011).
[21] P. Calabrese and J. Cardy, Journal of Statistical Mechanics: Theory and Experiment **2004**, P06002 (2004).
[22] R. Islam, R. Ma, P. M. Preiss, M. Eric Tai, A. Lukin, M. Rispoli, and M. Greiner, Nature **528**, 77 (2015).
[23] J. L. Cardy, Nuclear Physics B **240**, 514 (1984).
[24] I. Affleck and A. W. W. Ludwig, Phys. Rev. Lett. **67**, 161 (1991).
[25] L. Zhang and F. Wang, Phys. Rev. Lett. **118**, 087201 (2017).
[26] E. Brillaux, A. A. Fedorenko, and I. A. Gruzberg, Phys. Rev. B **109**, 174204 (2024).
[27] Y. Zou, Phys. Rev. B **105**, 165420 (2022).
[28] Z. Zhou, D. Gaiotto, Y.-C. He, and Y. Zou, SciPost Phys. **17**, 021 (2024).

[29] M. Oshikawa and I. Affleck, Nuclear Physics B **495**, 533 (1997).
[30] H. Li and F. D. M. Haldane, Phys. Rev. Lett. **101**, 010504 (2008).
[31] H.-L. Zhang, H.-Z. Li, S. Yang, and X.-J. Yu, Phys. Rev. A **109**, 062226 (2024).
[32] S. R. White, Phys. Rev. Lett. **69**, 2863 (1992).
[33] F. Verstraete and J. I. Cirac, Phys. Rev. B **73**, 094423 (2006).
[34] M. Fishman, S. R. White, and E. M. Stoudenmire, SciPost Phys. Codebases , 4 (2022).
[35] J. Gray, Journal of Open Source Software **3**, 819 (2018).
[36] V. Bergholm, J. Izaac, M. Schuld, *et al.*, "Pennylane: Automatic differentiation of hybrid quantum-classical computations," (2022), arXiv:1811.04968 [quant-ph].
[37] A. Paszke, S. Gross, F. Massa, *et al.*, in *Advances in Neural Information Processing Systems*, Vol. 32, edited by H. Wallach, H. Larochelle, A. Beygelzimer, F. d'Alché-Buc, E. Fox, and R. Garnett (Curran Associates, Inc., 2019).
[38] S.-X. Zhang, J. Allcock, Z.-Q. Wan, *et al.*, Quantum **7**, 912 (2023).
[39] M. Abadi, A. Agarwal, P. Barham, *et al.*, "TensorFlow: Large-scale machine learning on heterogeneous systems," (2015), software available from tensorflow.org.
[40] S. Xu, Z.-Z. Sun, K. Wang, *et al.*, Nature Physics **20**, 1469 (2024).
[41] K. Wang, W. Li, S. Xu, *et al.*, "Probing many-body bell correlation depth with superconducting qubits," (2024), arXiv:2406.17841 [quant-ph].
[42] Y. Li and S. C. Benjamin, Phys. Rev. X **7**, 021050 (2017).